

# Rheological and restoring force models regarding belt tensioner dynamic behavior: prediction & experiment.

**J. Bastien<sup>a</sup>, G. Michon<sup>b</sup>, L. Manin<sup>c</sup>, R. Dufour<sup>c</sup>**

<sup>a</sup> Laboratoire Mécatronique 3M, Équipe d'accueil A 3318

Université de Technologie de Belfort-Montbéliard, 90010 Belfort cedex, France

<sup>b</sup> Valeo Electrical Systems, 2 rue A. Boulle, 94000 Creteil, France

<sup>c</sup> Laboratoire de Dynamique des Machines et des Structures, UMR CNRS 5006, INSA de Lyon

Bât. Jean d'Alembert, 8 rue des Sciences, 69 621 Villeurbanne, France.

e-mail: [lionel.manin@insa-lyon.fr](mailto:lionel.manin@insa-lyon.fr)

## Abstract

The objective of this paper is to compare the Masing and modified Dahl model efficiency regarding the prediction of the hysteretic behavior of a belt tensioner used for automotive engines. A first experimental study with deflection imposed on the tensioner is carried out to identify hysteresis loop parameters for the two models. The models are then implemented in the general motion equations modeling the behavior of a belt - tensioner - mass system. The comparison between numerical and experimental results show that these two models perform satisfactorily and that the modified Dahl model is a little more efficient.

## 1 Introduction

The hysteretic behavior of components permits efficient passive control of mechanical systems but makes response prediction delicate due to their high non linearity [1, 2]. Vestroni and Noori in [2] and Visintin in [3] established an overview of hysteresis models. Rheological models and restoring force models are the two main categories widely used in mechanical engineering to predict those components behavior. The former provide damping and stiffness parameters, while the latter provide a restoring force to be introduced in the second member of the equations.

Here, the Masing model [4, 5] and the modified Dahl model [6, 7] are respectively the rheological and restoring force models selected for the current analysis. The classical Masing model composed of a spring parallel to a spring - dry friction system is modified in this study by adding a viscous damping element. The modified Dahl model originates from the Dahl and Duhem models and is based on a first differential equation that provides the time derivative of the restoring force from the velocity of the deflection and from the envelop curves of the hysteresis loop. The Masing model is governed by a non-smooth differential equation containing a multi-valued function while the Dahl model is governed by a smooth nonlinear dynamic equation. Consequently, the numerical integration schemes have to take into account these two typical characteristics to obtain a convergence. The efficiency of these two hysteresis models have to be tested to predict the hysteretic behavior of a belt tensioner.

Tensioners used in belt drive systems act as passive controllers by maintaining nominal tension in the slack span and reducing transverse vibration levels, see [8].

Satisfying technological challenges often leads to complicated design solution for tensioners, and involve considerably nonlinear behavior mainly due to stick-slip motion see for example [9, 10].

The Masing and modified Dahl models are described in detail in Section 2 and then applied to a belt tensioner of an automotive engine in Section 3, where an initial experimental set-up is used for identifying the model

parameters. Section 4 concerns the numerical and experimental investigations performed on a belt-tensioner-mass system in which tensioner behavior is either predicted by the two models studied. This section permits comparing the predicted and measured harmonic responses in order to discuss the models efficiencies.

## 2 The Models

In this section, two models describing the hysteretic behavior of a one degree of freedom mechanical system are presented. The behavior of the mechanical system studied can be analyzed via the progression of the restoring force versus the deflection.

The objective is to find the relation between a restoring force  $\mathcal{F}$  and a deflection  $u$ . It is assumed that after a transient phase  $[0, t_0]$ , the pair  $(u(t), \mathcal{F}(t))$  belongs to a periodic curve called hysteresis loop.

The modified Dahl model (see Section 2.1) and the Masing model with viscous damping (see Section 2.2) are used in the present investigation for modeling such behavior.

### 2.1 Theory of modified Dahl model

#### 2.1.1 Modified Dahl model

The model governed by Eq. (1) is presented and used in [6, 7] or in [11]; in this last reference, Eq. (1) was used to simulate the behavior of a belt tensioner.

$$\forall t \in [t_0, t_f], \quad \dot{\mathcal{F}}(t) = \begin{cases} \Lambda \dot{u}(t) \operatorname{sign}(h_u(u(t)) - \mathcal{F}(t)) |h_u(u(t)) - \mathcal{F}(t)|^\mu, & \text{if } \dot{u}(t) \geq 0, \\ -\Lambda \dot{u}(t) \operatorname{sign}(h_l(u(t)) - \mathcal{F}(t)) |h_l(u(t)) - \mathcal{F}(t)|^\mu, & \text{if } \dot{u}(t) \leq 0. \end{cases} \quad (1)$$

In this study, the authors consider the simple case where  $h_u$  and  $h_l$  are of polynomial form. Let  $a, b, d$  and  $e$  be real numbers, it is assumed that, for any  $u \in \mathbb{R}$ ,

$$h_u(u) = au + b, \quad h_l(u) = du + e. \quad (2)$$

#### 2.1.2 Analysis of hysteresis and identification of parameters $h_u$ , $h_l$ , $\mu$ and $\Lambda$ .

Parameter  $\Lambda$  characterizes the transient velocity between  $h_u$  and  $h_l$  while exponent  $\mu$  plays a predominant role in the loop orientation.

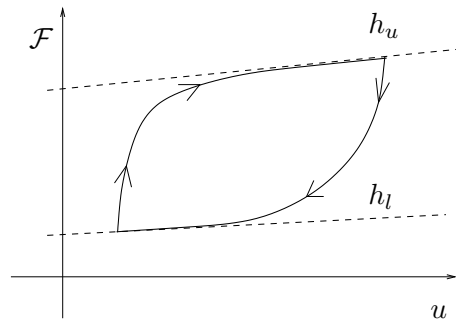


Figure 1: The force-deflection loop  $\Gamma$  for the modified Dahl model.

Figure 3: The two used multivalued maximal monotone graphs.

Considering the graph of the multivalued operator  $\sigma$  (see Fig. 3(a)) and its inverse graph  $\beta$  (see Fig. 3(b)), we obtain:

$$\beta(x) = \begin{cases} \emptyset & \text{if } x \in ]-\infty, -1[ \cup ]1, +\infty[, \\ \{0\} & \text{if } x \in [-1, 1], \\ \mathbb{R}_- & \text{if } x = -1, \\ \mathbb{R}_+ & \text{if } x = 1. \end{cases} \quad (3)$$

The graphs  $\beta$  and  $\sigma$  are maximal monotone (see for example [15]). The maximal monotone graphs  $\sigma$  and  $\beta$  are sub-differentials of proper semi-continuous convex functions  $|x|$  and  $\psi_{[-1,1]}$  defined by

$$\forall x \in \mathbb{R}, \quad \psi_{[-1,1]}(x) = \begin{cases} 0 & \text{if } x \in [-1, 1], \\ +\infty & \text{if } x \notin [-1, 1]. \end{cases} \quad (4)$$

Setting

$$w = u_s - l, \quad (5a)$$

$$\mathcal{F}_0 = k_0 l_0, \quad (5b)$$

$$\eta = \frac{\alpha}{k}. \quad (5c)$$

First, several equations similar to those presented in [4] are recalled. The constitutive law of the dry friction element is given by

$$f = \begin{cases} \tau \text{ with } \tau \in [-\alpha, \alpha], & \text{if } \dot{u}_t = 0, \\ -\alpha \text{Sign}(\dot{u}_t), & \text{if } \dot{u}_t \neq 0. \end{cases} \quad (6)$$

Then, by using the multivalued operator  $\sigma$  defined by (??) (see Fig. 3(a)), it is possible to write (6) in the form of the following differential inclusion:  $f \in -\alpha\sigma(\dot{u}_t)$ . By considering the constitutive laws of the springs, the dry friction element and the viscous damping element provide the following forces:

$$f_0 = -k_0(u - l_0), \quad (7a)$$

$$f = -k(u_s - l), \quad (7b)$$

$$f \in -\alpha\sigma(\dot{u}_t), \quad (7c)$$

$$f_1 = -c\dot{u}. \quad (7d)$$

The system equilibrium leads to

$$f + f_0 + f_1 + \mathcal{F} = 0, \quad (7e)$$

and the geometrical relation gives

$$u_s + u_t = u. \quad (7f)$$

By considering  $w$ ,  $\mathcal{F}_0$ ,  $\eta$ , defined by Eq. (5),  $w_0 = w(t_0) \in [-\eta, \eta]$  and  $\beta$  defined by (3), it can be proved that system (7) is equivalent to

$$\dot{w} + \beta\left(\frac{w}{\eta}\right) \ni \dot{u}, \quad (8a)$$

$$w(t_0) = w_0, \quad (8b)$$

$$\mathcal{F} = kw + k_0u + c\dot{u} - \mathcal{F}_0. \quad (8c)$$

### 2.2.2 Analysis of hysteresis and parameter identification.

As in [4], it is assumed that function  $\mathcal{F}$ , defined by Eq. (8c), is also periodic; under this assumption, it is proved that the loop  $(u, \mathcal{F})$  permits determining mechanical parameters of the Masing model with viscous damping.

Eq. (8c) can be rewritten as

$$\mathcal{F}_{\text{ep}}(t) = kw(t) + k_0u(t) - \mathcal{F}_0, \quad (9a)$$

$$\mathcal{F}_v(t) = c\dot{u}(t), \quad (9b)$$

$$\mathcal{F}(t) = \mathcal{F}_{\text{ep}}(t) + \mathcal{F}_v(t). \quad (9c)$$

The terms  $\mathcal{F}_{\text{ep}}$  and  $\mathcal{F}_v$  correspond to the elastoplastic part and to the viscous part of the model respectively.

It is now assumed that

$$u \text{ is } \tau\text{-periodic}; \quad (10a)$$

$$\begin{aligned} &\text{there exists } \tau_1, \tau_2 \text{ and } \tau_3 = \tau_1 + \tau, \text{ such that } u \text{ is strictly increasing on } [\tau_1, \tau_2] \\ &\text{and strictly decreasing on } [\tau_2, \tau_3]; \end{aligned} \quad (10b)$$

$$u \in C^2([t_0, t_f]), \quad (10c)$$

and setting

$$u_{\min} = \min(u), \quad u_{\max} = \max(u). \quad (11)$$

If no damping is considered, then  $\mathcal{F}_v$  is nil and we can prove under assumption (10a), as in [4], that the pair  $(u, \mathcal{F})$  versus time plots a hysteresis loop. This loop represents a clockwise oriented parallelogram as  $t$  is increasing on the interval  $[t_0, t_f]$ . A direct correspondence exists between the six parallelogram parameters and the six system parameters  $u_{\min}$ ,  $u_{\max}$ ,  $k_0$ ,  $k$ ,  $\alpha$  and  $\mathcal{F}_0$ , thus permitting their identification.

On the other hand, when damping is considered, the pair  $(u, \mathcal{F})$  does not plot a hysteresis loop, in the classical sense of [3]. Indeed, the pair  $(u, \mathcal{F}_{\text{ep}})$  plots a hysteresis loop called the dry skeleton. However, since the second term  $\mathcal{F}_v$  depends on the deflection history, the pair  $(u, \mathcal{F}_v)$  does not draw a hysteresis loop. Moreover, with  $c \neq 0$ , the identification of the mechanical parameters is still possible due to geometrical data of the loop .

The loop studied  $(u(t), \mathcal{F}(t))$  for  $t$  belonging to  $[t_0, t_f]$  is symmetric and only the upper half part of this curve is studied, as in [4]. In this last part  $[\tau_1, \tau_2]$ ,  $u$  is strictly increasing and there is a bijection  $\psi_+$  such that, for any  $t \in [\tau_1, \tau_2]$ ,  $t = \psi_+(u(t))$ ; moreover,  $u(\tau_1) = u_{\min}$  and  $u(\tau_2) = u_{\max}$ . By considering  $\mathcal{G}_+ = \dot{u} \circ \psi_+$ , we obtain

$$\forall t \in [\tau_1, \tau_2], \quad \dot{u}(t) = \mathcal{G}_+(u(t)), \quad (12)$$

and Eq. (9) can be rewritten as

$$\forall u \in [u_{\min}, u_{\max}], \quad \mathcal{F}_v(u) = c\mathcal{G}_+(u), \quad (13)$$

and

$$\forall u \in [u_{\min}, u_{\max}], \quad \mathcal{F}(u) = \mathcal{F}_{\text{ep}}(u) + \mathcal{F}_v(u), \quad (14)$$

where

$$\mathcal{F}_{\text{ep}}(u) = kw(u) + k_0u - \mathcal{F}_0, \quad (15)$$

where  $w$  depends only on  $u$  via the differential inclusion (8a).

If the deflection amplitude is large enough, then it exists  $\tau_4 \in [\tau_1, \tau_2]$  so that

$$w(\tau_1) = -\eta, \quad w(\tau_4) = \eta. \quad (16)$$

Henceforth, we consider

$$t_A = \tau_1, \quad t_B = \tau_4, \quad t_C = \tau_2, \quad (17a)$$

$$u_A = u(\tau_1), \quad u_B = u(\tau_4), \quad u_C = u(\tau_2), \quad (17b)$$

$$\mathcal{F}_A = \mathcal{F}(u_A), \quad \mathcal{F}_B = \mathcal{F}(u_B), \quad \mathcal{F}_C = \mathcal{F}(u_C). \quad (17c)$$

On the interval  $[\tau_1, \tau_4]$ , the dry friction element sticks and the model sketched in Fig. 2 is identical to the association of a spring with stiffness  $k + k_0$  and a damping viscous element. After computation, thanks to Eq. (16), we obtain

$$\forall u \in [u_A, u_B], \quad \mathcal{F}(u) = (k + k_0)u - \mathcal{F}_0 - k(u_A + \eta) + c\mathcal{G}_+(u). \quad (18a)$$

On the contrary, on the interval  $[\tau_4, \tau_2]$ , the dry friction element slips and the model sketched on Fig. 2 is identical to the association of a spring with stiffness  $k_0$  and a damping viscous element. After computation, we obtain

$$\forall u \in [u_B, u_C], \quad \mathcal{F}(u) = k_0u + k\eta - \mathcal{F}_0 + c\mathcal{G}_+(u). \quad (18b)$$

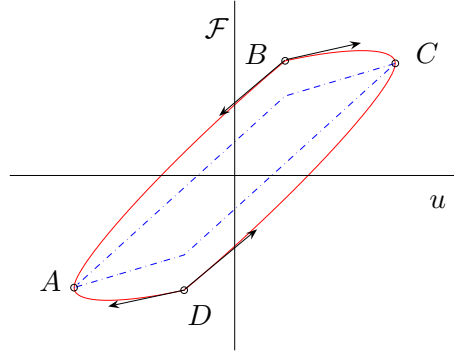


Figure 4: The force-deflection loop  $\Gamma$  for the Masing model with viscous damping (solid line), the dry skeleton (dot-dashed line), and the corners  $A$ ,  $B$ ,  $C$  and  $D$ .

By using Eqs. (18), the shape of the loop  $(u, \mathcal{F})$  is given in the Fig. 4, where the dry skeleton corresponds to the pair  $(u, \mathcal{F}_{\text{ep}})$ . Corners  $A$  and  $C$  represent slip stick state change whereas the corners  $B$  and  $D$  represent stick slip state change.

For  $u = u_A$ ,  $\dot{u}$  is equal to zero and then  $\mathcal{G}_+(u_A)$  is equal to zero; thus, Eqs. (18) gives

$$\mathcal{F}_A = (k + k_0)u_A - \mathcal{F}_0 - k(u_A + \eta). \quad (19a)$$

and

$$\mathcal{F}_C = k_0u_C + k\eta - \mathcal{F}_0. \quad (19b)$$

With Eq. (18a), for  $u = u_A$  and  $u = u_B$ , we obtain

$$u_B - u_A = 2\eta. \quad (19c)$$

By definition,

$$u_A = u_{\min}, \quad u_C = u_{\max}. \quad (19d)$$

Let  $p_B^+$  and  $p_B^-$  be the right and left derivatives of  $\mathcal{F}$  according to  $u$  at point  $u_B$ ; According to Eq. (18) and since  $u$  is of class  $C^1$ :

$$p_B^+ = k_0 + c\mathcal{G}'_+(u_B). \quad (20a)$$

$$p_B^- = k + k_0 + c\mathcal{G}'_+(u_B). \quad (20b)$$

Thanks to assumption (10c),  $\mathcal{G}'_+$  is continuous in  $u_B$  and we obtain

$$p_B^- - p_B^+ = k. \quad (21)$$

Moreover,

Point  $B$  is the unique point of the upper part of the loop  $(u, \mathcal{F})$

where the derivative is not continuous. (22)

Similarly, on the decreasing part of the loop, the same approach is developed. We consider, if  $u$  is strictly decreasing,  $t = \psi_-(u(t))$  and we obtain

$$\forall u \in [u_D, u_C], \quad \mathcal{F}(u) = (k + k_0)u - \mathcal{F}_0 - k(u_C - \eta) - c\mathcal{G}_-(u). \quad (23a)$$

$$\forall u \in [u_A, u_D], \quad \mathcal{F}(u) = k_0u - k\eta - \mathcal{F}_0 - c\mathcal{G}_-(u). \quad (23b)$$

As in [4], the following equations remain true and permit parameter identification:

$$u_{\min} = u_A, \quad (24a)$$

$$u_{\max} = u_C, \quad (24b)$$

$$k = p_B^- - p_B^+, \quad (24c)$$

$$\alpha = \frac{k}{2}(u_B - u_A), \quad (24d)$$

$$k_0 = \frac{\mathcal{F}_C - \mathcal{F}_A - 2\alpha}{u_C - u_A}, \quad (24e)$$

$$\mathcal{F}_0 = k_0u_A - \alpha - \mathcal{F}_A. \quad (24f)$$

These equations are obtained by Eqs. (19) and (21).

However, the value of  $c$  must be determined. A similar method to that of [11] is used to estimate the value of  $\Lambda$  for  $\mu = 1$ . By equating the calculated and measured energies dissipated by the viscous damping element, *i.e.* the inside area of the loops  $(u, c\dot{u})$ , we can write Eq. (9) as:

$$\mathcal{F} - (kw + k_0u - \mathcal{F}_0) = \mathcal{F} - \mathcal{F}_{\text{ep}} = \mathcal{F}_v = c\dot{u} = c\mathcal{G}_+,$$

or thanks to Eqs. (18) and (23),

$$\forall u \in [u_A, u_B], \quad \mathcal{F}(u) - ((k + k_0)u - \mathcal{F}_0 - k(u_A + \eta)) = c\mathcal{G}_+(u), \quad (25a)$$

$$\forall u \in [u_B, u_C], \quad \mathcal{F}(u) - (k_0u + k\eta - \mathcal{F}_0) = c\mathcal{G}_+(u), \quad (25b)$$

$$\forall u \in [u_D, u_C], \quad \mathcal{F}(u) - ((k + k_0)u - \mathcal{F}_0 - k(u_C - \eta)) = -c\mathcal{G}_-(u), \quad (25c)$$

$$\forall u \in [u_A, u_D], \quad \mathcal{F}(u) - (k_0u - k\eta - \mathcal{F}_0) = -c\mathcal{G}_-(u). \quad (25d)$$

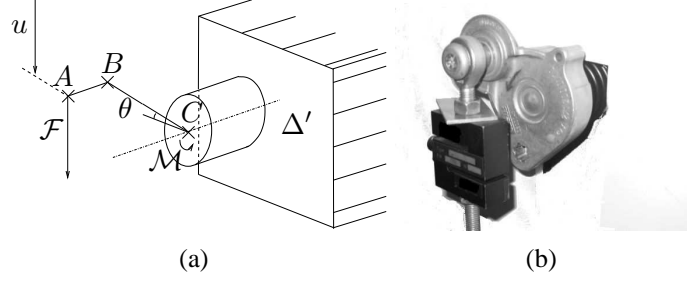


Figure 5: Tensioner schemes and pictures: (a-b).

The two functions  $\mathcal{G}_+$  and  $\mathcal{G}_-$  are known and the energy dissipated  $\mathcal{E}$  has the following expression:

$$\mathcal{E} = c \int_{u_{\min}}^{u_{\max}} \mathcal{G}_+(u) - \mathcal{G}_-(u) du = c \left( \int_{\substack{t_A \\ u \text{ increasing}}}^{t_C} \dot{u}^2(t) dt - \int_{\substack{t_C \\ u \text{ decreasing}}}^{t_A} \dot{u}^2(t) dt \right). \quad (26)$$

If  $u$  is defined by

$$\forall t, \quad u(t) = x_0 + x_1 \sin(\Omega t + \phi), \quad (27)$$

Eq. (26) yields

$$\mathcal{E} = \pi x_1^2 \Omega c. \quad (28)$$

The value of damping  $c$  is determined for pulsation  $\Omega$ . In Section 4, the value of  $c$  will be used, but pulsation  $\Omega_0$  will be equal to  $\Omega$ . It is now assumed that the shape of the loop  $(u, \mathcal{F})$  does not depend on pulsation  $\Omega_0$ . In Section 4, value  $c_0$  will be used:

$$c_0 = \frac{\Omega}{\Omega_0} c, \quad (29)$$

where  $c$  is given by (28).

### 3 Experimental investigation and parameter identification

The tensioner is composed of three parts, see Fig. 5: Part 1 is a solid (Idler pulley) that rotates around axis  $\Delta = (AB)$  of part 2; part 2 is the tensioner arm  $ABC$ , that rotates around the fixed axis  $\Delta'$  of part 3, bolted to the reference part 4 (i.e an engine for automotive applications). All the parts are considered as rigid bodies. The pin joint of axis  $\Delta'$  between parts 2 and 3 includes a torsion spring and friction components that cause dry and lubricated contact forces, and a moment between parts 2 and 3. The phenomena involved result in highly non linear behavior of the joint.

An experimental set up has been designed for identifying the belt tensioner model parameters. The idler pulley is removed and segment  $AB$  is connected to a rigid bar that subjects a vertical alternative displacement on point  $A$ . The vertical components of point  $A$ , displacement  $u(t)$ , and of force  $\mathcal{F}$  are considered positive when oriented toward the ground, since in use, the tensioner is always preloaded. Force  $\mathcal{F}$  remains positive.

The displacements are measured using laser optical sensors, while the forces are measured with load cells. Data acquisition is performed simultaneously with a sample frequency  $f_{\text{sto}} = 5000$  Hz. The measurements can be filtered to remove measurement noise.

#### 3.1 Experimental set-up for identifying the parameters of the models

An alternative vertical displacement is imposed on point  $A$ , defined by Eq. (27), with

$$\Omega = 9.4 \text{ rad/s}, \quad \phi = 4.8 \text{ rad}, \quad x_0 = 5.4 \cdot 10^{-4} \text{ m}, \quad x_1 = 5.2 \cdot 10^{-4} \text{ m}. \quad (30)$$

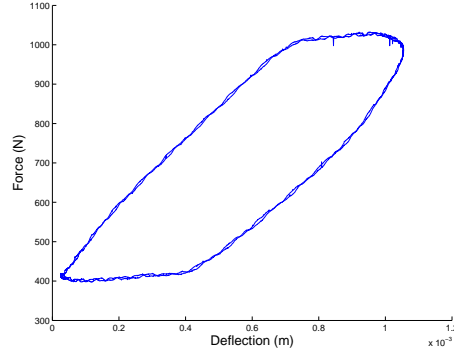


Figure 6: Measured loop  $(u, \mathcal{F})$ , small deflection amplitude.

After a transient state (start from initial position), a steady hysteretic loop is observed as shown on Fig. 6 and the measured force  $\mathcal{F}$  versus time is periodic.

In [11], the authors have shown that the Dahl modified model parameters are dependent on  $x_0$  and to a lesser extent on  $\Omega$ . This dependency is not considered here: The values of  $x_0$  and  $x_1$ , given by Eq. (30), have been chosen so that the  $\max(u) - \min(u)$  range, observed on Fig. 6 should be similar to that observed in Section 4. Moreover, it is supposed that the characteristics of the models studied depend on the  $\max(u) - \min(u)$  range but do not depend on frequency forcing  $\Omega$ .

## 3.2 Identification of the model parameters

### 3.2.1 Modified Dahl model

In order to identify the parameters defining  $h_u$  and  $h_l$ , the method of Section 2.1.2 is used: as in [11], we use the fact that  $h_u$  and  $h_l$  represent the upper and lower envelop curves of the hysteretic loop  $\Gamma$  to which the pair  $(u(t), \mathcal{F}(t))$  belongs when  $t$  describes  $[t_0, t_f]$ . For the next development it is considered that  $u$  is defined by Eqs. (27) and (30).

From the analysis of the measured loop represented in Fig. 6, the envelop curves  $h_u$  and  $h_l$  can be considered as straight lines and therefore the values of  $a$ ,  $b$ ,  $d$  and  $e$  are determined using the mean squares approximation method (see Fig. 7):

$$a = 7.146 \cdot 10^4 \text{ N/m}, \quad b = 9.596 \cdot 10^2 \text{ N}, \quad d = 5.322 \cdot 10^4 \text{ N/m}, \quad e = 3.972 \cdot 10^2 \text{ N}. \quad (31)$$

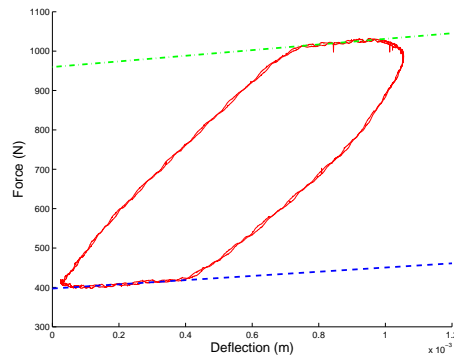


Figure 7: Identification of the envelop curves  $h_u$  (dot-dashed line) and  $h_l$  (dashed line), measured loop (solid line).

In order to use the modified Dahl model, the initial conditions  $(t_0, \mathcal{F}_0)$  are determined by choosing an arbitrary point of the loop:

$$t_0 = 1.988 \cdot 10^{-1} \text{ s}, \quad \mathcal{F}_0 = 1.009 \cdot 10^3 \text{ N}. \quad (32)$$

Moreover, using the results of Section 2.1.2 and after several numerical iterations, the optimal values of parameters  $\Lambda$  and  $\mu$  are determined:

$$\Lambda = 117355, \quad \mu = 0,37. \quad (33)$$

### 3.2.2 Masing model with viscous damping

In order to identify the parameters of the Masing model with viscous damping i.e.  $\{u_{\min}, u_{\max}, k, k_0, \alpha, \mathcal{F}_0, c\}$ , the results of section 2.2.2 are applied to the experimental loop represented on Fig. 6.

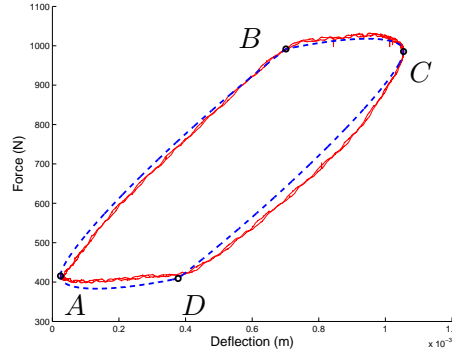


Figure 8: Predicted (Masing model with viscous damping, dashed line) and measured (solid line) loops and the corners  $A$ ,  $B$ ,  $C$  and  $D$ .

As shown on Fig. 8, the numerical values of  $u_A, u_B, u_C, \mathcal{F}_A, \mathcal{F}_C, p_B^-,$  and  $p_B^+$  are determined, and thanks to Eqs. (24) and (28) we obtain the following:

$$u_{\min} = 2 \cdot 10^{-5} \text{ m}, \quad u_{\max} = 1.05 \cdot 10^{-3} \text{ m}, \quad (34a)$$

$$k = 4.84 \cdot 10^5 \text{ N/m}, \quad k_0 = 2.34 \cdot 10^5 \text{ N/m}, \quad \alpha = 1.63 \cdot 10^2 \text{ N}, \quad \mathcal{F}_0 = -5.73 \cdot 10^2 \text{ N}. \quad (34b)$$

$$c = 1.93 \cdot 10^4 \text{ Ns/m}. \quad (34c)$$

As in Section 3.2.1, the initial conditions  $(t_0, w_0 = w(t_0))$  are determined choosing an arbitrary point of the loop:

$$t_0 = 1.55 \cdot 10^{-2} \text{ s}, \quad w(t_0) = -3.24 \cdot 10^{-4} \text{ m}. \quad (35)$$

### 3.3 Comparison of the results obtained with the modified Dahl and Masing models and with the experiment

The previous identification permits predicting the force for an imposed deflection; Numerical and analytical computations were performed for the modified Dahl model and the Masing model.

The force deflection loop  $u \mapsto \mathcal{F}$  is plotted on Fig. 9. By comparing the force deflection loops, it appears that the stick slip state transition is modeled differently. Indeed, for the Dahl model, the stick slip transition

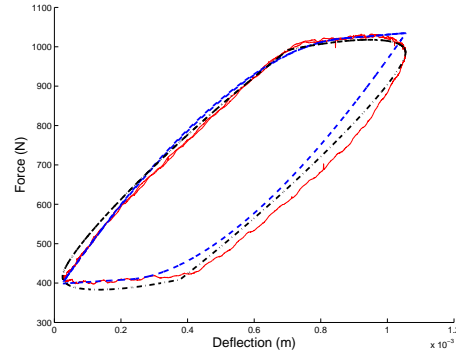


Figure 9: Identification part: load  $\mathcal{F}$  versus deflection  $u$  measured (solid line) and predicted with the modified Dahl model (dashed line) and with the Masing model (dot-dashed line).

is continuous through it is not for the slip stick transition. This is the contrary for the Masing model with viscous damping. In addition, the higher the viscous damping, the smoother the slip stick transition will be.

Both experimental and numerical results are presented in Figs. ?? and 9. Good agreement can be observed between the two theoretical models and also between each model and the experiment performed to validate the models used and their identification.

## 4 Comparison, validation and prediction

In the previous section, the Modified Dahl and Masing models were formulated for the belt tensioner. The tensioner is now a part of a mechanical system subjected to a variable load excitation. The purpose is to test the models efficiency considering a multi-degree of freedom system and an experimental investigation. Each tensioner model is implemented in the system motion equations that are solved numerically. The predicted and measured results are compared.

### 4.1 Equations of motion for the system

#### 4.1.1 System description

The dynamic system considered is composed of the previously studied tensioner, a poly-V belt and a mass (see Fig. 10). The tensioner base is fixed on a rigid frame. Its idler pulley of mass  $m_2$  has a belt wrapped around it. The two adjacent belt spans are joined at their other end and connected to a mass  $m_1$ . The mass  $m_1$  is excited by the imposed force  $f$  generated by an electro-dynamic shaker (see Figs. 10). Two Displacements  $u_1$  and  $u_2$  (see Fig. ??) of the two masses are measured with laser-optical displacement sensors. The transmitted force  $f$  is measured with a piezo-electric load sensor, and the belt tension is measured with an S-shape load sensor. In this two degrees of freedom system, mass  $m_1$  is used both for the tensioner preload and for the system dynamics.

#### 4.1.2 System equations

Let  $u_1$  and  $u_2$  be the vertical displacements of masses 1 and 2, along the  $x$  axis, both positive oriented downward. As in section 3,  $\mathcal{F}$  is the force exerted by the tensioner, it is positive oriented upward. Force  $f$  is

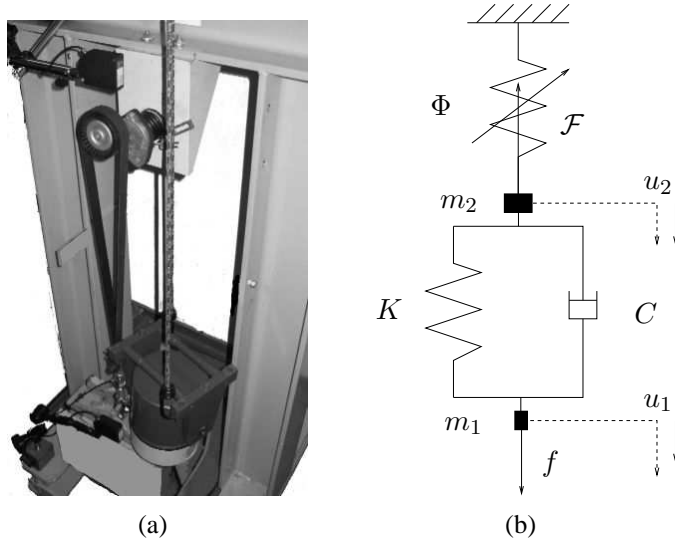


Figure 10: Experimental set-up: Belt-tensioner-mass system.

positive oriented downward. Let  $T/2$  be the tension in each belt span. Due to the ratio between the radius of the pulley and the belt span lengths, it is assumed that tension  $T$  is oriented vertically.

The gravity constant is noted as  $g$  and equations governing the complete system are given by:

- The belt behavior law, by considering the belt as a spring-damper of stiffness  $K$  and equivalent viscous damping  $C$ :

$$T(t) = K(u_1(t) - u_2(t)) + C(\dot{u}_1(t) - \dot{u}_2(t)) + \mathcal{T}_0, \quad (36a)$$

where  $\mathcal{T}_0$  is related to the initial belt tension.

- The dynamic equilibrium of the tensioner pulley projected along the vertical axis  $x$ , by neglecting effects on the horizontal axis:

$$m_2\ddot{u}_2(t) = T(t) - \mathcal{F}(t) + m_2g. \quad (36b)$$

- The dynamic equilibrium of the lower mass projected along the vertical axis  $x$ , by neglecting effects on the horizontal axis:

$$m_1\ddot{u}_1(t) = -T(t) + f(t) + m_1g. \quad (36c)$$

- Initial data at  $t_0$  for  $u_1$  and  $u_2$ :

$$u_1(t_0) = u_{1,0}, \quad \dot{u}_1(t_0) = \dot{u}_{1,0}, \quad u_2(t_0) = u_{2,0}, \quad \dot{u}_2(t_0) = \dot{u}_{2,0}. \quad (36d)$$

- The relation between force  $\mathcal{F}$  and displacement  $u_2$  is written formally as:

$$\mathcal{F} = \Phi(u_2), \quad (36e)$$

where  $\Phi$  is an operator.

Belt stiffness  $K$  and damping  $C$  are obtained by using an experimental model analysis non presented here. The parameter values of the system are fixed:

$$m_1 = 73.84 \text{ kg}, \quad m_2 = 0.15 \text{ kg}, \quad K = 560000 \text{ N/m}, \quad C = 160 \text{ Ns/m}, \quad g = 9.81 \text{ m/s}^2. \quad (37)$$

The initial conditions are chosen arbitrarily

$$t_0 = 1,6 \cdot 10^{-3}, \quad u_{1,0} = 0, \quad \dot{u}_{1,0} = 0, \quad u_{2,0} = 0, \quad \dot{u}_{2,0} = 0, \quad (38)$$

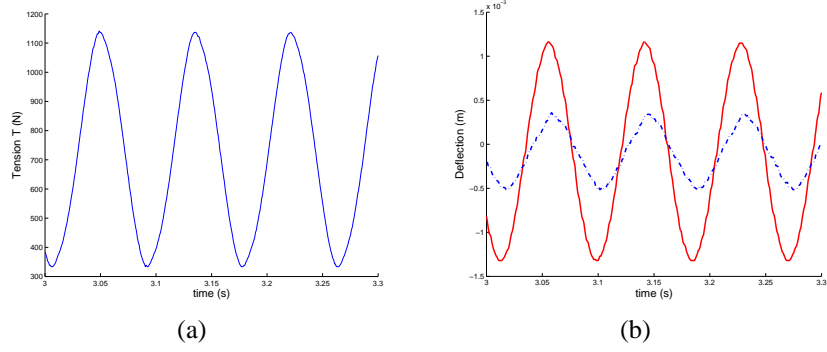


Figure 11: Measured curves  $T$  (a),  $u_1$  (b, solid line) and  $u_2$  (b, dot-dashed line) versus time (on time interval  $[3, 3.3]$ ).

#### 4.1.3 Application of the modified Dahl model

Applying the modified Dahl model for the tensioner implemented in the system, consists in replacing  $u$  by  $u_2$  in Eqs. (1):

$$\dot{\mathcal{F}}(t) = \begin{cases} \Lambda \dot{u}_2(t) \text{sign}(h_u(u_2(t)) - \mathcal{F}(t)) |h_u(u_2(t)) - \mathcal{F}(t)|^\mu, & \text{if } \dot{u}_2(t) \geq 0, \\ -\Lambda \dot{u}_2(t) \text{sign}(h_l(u_2(t)) - \mathcal{F}(t)) |h_l(u_2(t)) - \mathcal{F}(t)|^\mu, & \text{if } \dot{u}_2(t) \leq 0, \end{cases} \quad (39)$$

$$\mathcal{F}(t_0) = \mathcal{F}_0. \quad (40)$$

Finally, it is necessary to solve the system formed by Eqs. (36a), (36b), (36c), (39) and initial conditions (36d) and (40). It is admitted that  $u_1$ ,  $u_2$ ,  $T$  and  $\mathcal{F}$  exist and are unique.

#### 4.1.4 Application of the Masing model with viscous damping

For the Masing model with viscous damping, replacing  $u$  by  $u_2$  transforms Eq. (8) in:

$$\dot{w} + \beta \left( \frac{w}{\eta} \right) \ni \dot{u}_2, \text{ on } [t_0, t_f] \quad (41a)$$

$$w(t_0) = w_0, \quad (41b)$$

$$\mathcal{F} = kw + k_0 u_2 + c \dot{u}_2 - \mathcal{F}_0, \text{ on } [t_0, t_f]. \quad (41c)$$

Finally, we obtain the system of Eqs. (36a), (36b), (36c), (41a), (41c), and initial conditions (36d) and (41b). These equations are written as a differential inclusion of the first order studied in [4, 15].

## 4.2 Predicted and measured responses

In this section, the predicted and measured responses of the multi degrees of freedom system are presented and compared (see Figs. 11). No transient phase is observed for the measured responses.

The value of force  $\mathcal{F}$  is reached using Eq.(36b) which gives

$$T(t) - \mathcal{F}(t) = m_2(\ddot{u}_2(t) - g).$$

and since  $m_2$  defined by (37) is negligible compared to  $m_1$ , it leads to:

$$T(t) \approx \mathcal{F}(t). \quad (42)$$

The two theoretical models give satisfactory results. The short time deviation  $\Delta t$  is due to the unknown initial conditions. For the same reason, there are also shifts  $\Delta u_1$  and  $\Delta u_2$  between the experimental and computed curves  $u_1$  and  $u_2$ ;  $\Delta u_1$  and  $\Delta u_2$  are determined so that the mean values of  $u_1$  and  $u_2$  are nil. Finally, displacement shifts  $\Delta u_1$ ,  $\Delta u_2$  and  $\Delta t$  are introduced in the model and function  $\mathcal{F}$  is plotted versus the deflection  $u_2$  (see Fig. 12).

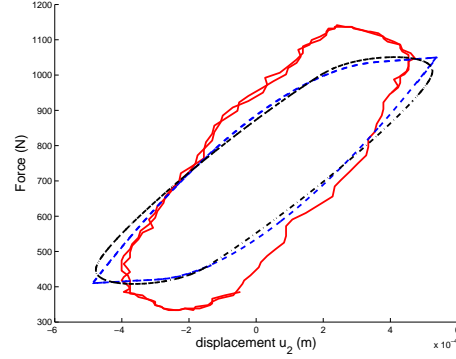


Figure 12: Validation part: force  $\mathcal{F}$  versus deflection  $u_2$  predicted with the modified Dahl model (dashed line) and with the Masing model (dot-dashed line), and measured (solid line).

### 4.3 Global behavior

The comparisons of the results on Fig. 12 shows that there is a small difference between the measured and predicted loops. This is probably due to the fact that the mechanical parameters of the two models studied depend on the  $\max(u_2) - \min(u_1)$  displacement range. According to Section 3.1, the parameters of the modified Dahl and Masing models with viscous damping depend on  $u_2$  and the analysis can be improved.

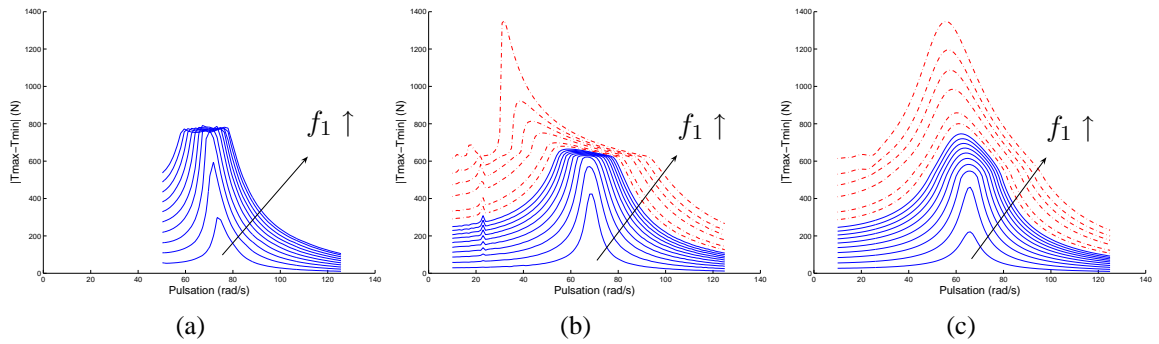


Figure 13: Prediction part: Amplitude  $|\max(T) - \min(T)|$  versus pulsation  $\Omega$  for several values of  $f_1$  for the experiment (a), the modified Dahl model (b) and the Masing model with viscous damping (c) for  $f_1$  defined by (43c) (solid curves) and for  $f_1$  defined by (44) (dot-dashed curves), with  $f_1$  increasing in the direction of the arrow.

Finally some values of  $|\max(T) - \min(T)|$  versus forcing pulsation  $\Omega$  are measured for several values of  $f_1$

(and with  $f_0$  and  $\phi$  fixed). For each value of  $\Omega$ ,  $c_0$  is defined by (29). We choose

$$t_0 = 17 \text{ s}, \quad t_f = 20 \text{ s}, \quad h = 10^{-5} \text{ s}, \quad (43a)$$

$$f_0 = 0, \quad \phi = 0, \quad (43b)$$

$$f_1 \in [13, 27, 41, 54, 67, 79, 90, 100, 110, 120], \quad (43c)$$

$$\Omega \in [10, 125] \text{ (with 116 values arranged linearly)}. \quad (43d)$$

Measured and predicted responses are plotted in Fig. 13. The computed frequency response represented in this figure is obtained after a series of calculations in the time domain: each point of a frequency response curve corresponds to the tension fluctuation amplitude calculated when steady state is reached for a given frequency and excitation amplitude. The dot-dashed curves correspond to the predicted results obtained for higher excitation force amplitudes not obtained experimentally:

$$f_1 \in [140, 160, 200, 230, 260, 300]. \quad (44)$$

It can be observed experimentally that even if the excitation force amplitude increases, the resulting belt tension variation is bounded within a frequency range. This phenomenon is predicted better if the tensioner is modeled with the modified Dahl model rather than with the Masing model with viscous damping.

The system behavior observed in Figs. 13 is similar to that described in [16, 17] For small forcing amplitudes, the tensioner is stuck. For high forcing amplitudes, it mainly slips.

## 5 Conclusion

This paper has described in detail two different models usually used to reproduce hysteretic behavior.

It has been shown that the stick-slip behavior exhibited of a belt tensioner can be modeled either by the Masing model or the modified Dahl model.

Model parameters have been identified experimentally with an imposed deflection and a low forcing frequency. The numerical and experimental investigations carried out on a belt-tensioner-mass system in a larger forcing frequency range have shown that the use of these two models is satisfactory in the time history and frequency domains.

It should be noted that particular attention must be given to the use of the numerical schemes in order to make the predicted responses reliable.

## References

- [1] W. Lacarbonara and F. Vestroni. Nonclassical responses of oscillators with hysteresis. *Nonlinear Dynamics*, 32:235–258, 2003.
- [2] F. Vestroni and M. Noori. Hysteresis in mechanical systems - modeling and dynamic response. *International Journal of Non-Linear Mechanics*, 37:1261–1262, 2002.
- [3] A. Visintin. *Differential models of hysteresis*. Springer-Verlag, Berlin, 1994.
- [4] Jérôme Bastien, Michelle Schatzman, and Claude-Henri Lamarque. Study of some rheological models with a finite number of degrees of freedom. *Eur. J. Mech. A Solids*, 19(2):277–307, 2000.
- [5] R. Fougères and F. Sidoroff. The evolutive masing model and its application to cyclic plasticity and ageing. *Nuclear Engineering and Design*, 114:273–284, 1989.

- [6] A. Al Majid and R. Dufour. Formulation of a hysteretic restoring force model. Application to vibration isolation. *Nonlinear Dynamics*, 27:69–85, 2002.
- [7] A. Al Majid and R. Dufour. Harmonic response of a structure mounted on an isolator modelled with a hysteretic operator: Experiment and prediction. *Journal of Sound and Vibration*, 277:391–403, 2004.
- [8] R.S. Beikmann, N.C. Perkins, and A.G. Ulsoy. Design and analysis of automotive belt drive systems for steady state performance. *ASME Journal of Mechanical Design*, 119:162–168, 1997.
- [9] R.G. Parker. Efficient eigensolution, dynamic response, and eigensensitivity of serpentine belt drives. *Journal of Sound and Vibration*, 270:15–38, 2004.
- [10] M.J. Leamy and N.C. Perkins. Nonlinear periodic response of engine accessory drives with dry friction tensioners. *ASME Journal of Vibration and Acoustics*, 120:909–916, 1998.
- [11] G. Michon, L. Manin, and R. Dufour. Hysteretic behavior of a belt tensioner: Modeling and Experimental investigation. *Journal of Vibration and Control*, 11(9):1147–1158, 2005.
- [12] Manuel D. P. Monteiro Marques. An existence, uniqueness and regularity study of the dynamics of systems with one-dimensional friction. *European J. Mech. A Solids*, 13(2):277–306, 1994.
- [13] David E. Stewart. Rigid-body dynamics with friction and impact. *SIAM Rev.*, 42(1):3–39 (electronic), 2000.
- [14] Jérôme Bastien and Michelle Schatzman. Numerical precision for differential inclusions with uniqueness. *M2AN Math. Model. Numer. Anal.*, 36(3):427–460, 2002.
- [15] Haïm Brezis. *Opérateurs maximaux monotones et semi-groupes de contractions dans les espaces de Hilbert*. North-Holland Publishing Co., Amsterdam, 1973. North-Holland Mathematics Studies, No. 5. Notas de Matemática (50).
- [16] F. D’Ambrosio, E. Chatelet, and G. Jacquet. Influence of contact states on the dynamic behavior of rubbing structures. In *Proceedings of IGTI 2005, ASME Turbo Expo*, Reno-Tahoe, Nevada, USA, June 6-9 2005.
- [17] K.Y. Sanliturk and D.J. Ewins. Modelling two-dimensional friction contact and its application using harmonic balance method. *Journal of Sound and Vibration*, 193(2):511–523, 1996.